

Toward Microstructure-Informed Reduced-Order Modeling of Fatigue Initiation in a Titanium Skin Panel Subjected to Thermo-Mechanical Loading

Min Lin *

University of Wyoming, Laramie, Wyoming, 82071, US

Yang Liu †

Imperial College London, London, SW72AZ, UK

Caglar Oskay ‡

Vanderbilt University, Nashville, Tennessee, 37240, US

Xiang Zhang §

University of Wyoming, Laramie, Wyoming, 82071, US

In this work, we present a multiscale reduced-order modeling framework to simulate the response of a generic titanium skin panel structure subjected to thermo-mechanical loading associated with high-speed flight, which could be potentially used for microstructure-informed fatigue damage initiation prediction in Aerostructures. The formulation is based on the eigenstrain-based reduced-order homogenization model (EHM) for polycrystal plasticity the authors have developed over the past few years. New developments in this manuscript accounts for thermal strains as well as temperature dependent material properties and evolution laws. In this framework, the material microstructure (i.e., at the scale of a polycrystalline representative volume element (RVE)) and underlying microstructural mechanisms are directly incorporated and fully coupled with a structural analysis that involves thermo-mechanical loading. This formulation allows concurrently probing the response at the structural scale and the material microscale, enabling microstructure-informed structural scale fatigue analysis. The model is calibrated based on a series of uniaxial tension tests of Ti-6242S at a wide range of temperatures and two different strain rates, and then adopted to study the response of a generic aircraft skin panel in high-speed flight condition. The analysis focuses on demonstrating the capability of the model to predict not only the structural scale response, but simultaneously the microscale response, and its potential for microstructure-informed fatigue damage initiation prediction.

*Graduate student, Department of Mechanical Engineering, email: mlin4@uwoyo.edu

†Postdoctoral Fellow, Department of Materials, email: yang.liu@imperial.ac.uk

‡Professor, Department of Civil Engineering, email: caglar.oskay@vanderbilt.edu, member AIAA

§Assistant Professor, Department of Mechanical Engineering, corresponding author email: xiang.zhang@uwoyo.edu, member AIAA

Nomenclature

$\mathbf{x}, \mathbf{y}; \zeta$	=	Coordinates of the macro- and microscale domain; scale separation parameter
$\bar{\mathbf{u}}, \bar{T}$	=	macroscopic displacement and temperature
$\bar{\boldsymbol{\epsilon}}, \bar{\boldsymbol{\sigma}}, \bar{\mathbf{b}}$	=	macroscopic strain, stress and body force
$\bar{\rho}, \bar{c}, \bar{K}$	=	Homogenized density, specific heat and thermal conductivity at the macroscale
$\boldsymbol{\epsilon}^{(\alpha)}, \boldsymbol{\mu}^{(\alpha)}, \boldsymbol{\sigma}^{(\alpha)}$	=	strain, inelastic strain and stress of part α
$\dot{\gamma}^{s(\alpha)}, s^{s(\alpha)}, \tau^{s(\alpha)}, Z^{s(\alpha)}$	=	slip rate, strength, resolved shear stress and Schmid factor of the s-th slip system of part α
$s_0^{s(\alpha)}, s_{\text{for}}^{s(\alpha)}, s_{\text{deb}}^{s(\alpha)}$	=	initial slip resistance, and slip resistance due to forest dislocation and dislocation debris
$\rho_{\text{fwd}}^{s(\alpha)}, \rho_{\text{rev}}^{s+(\alpha)}, \rho_{\text{rev}}^{s-(\alpha)}$	=	dislocation densities of the s-th slip system of part α
$\mathbf{A}, \mathbf{P}, \boldsymbol{\mathcal{A}}, \mathbf{M}$	=	coefficient tensors
\mathbf{I}	=	Identity tensor
Superscripts		
$s; \alpha, \beta$	=	slip system index; part number
Subscripts		
for; deb; tot	=	forest dislocation, dislocation debris; total dislocation density
i, j, k, l, m, n	=	index

I. Introduction

AEROSTRUCTURES are exposed to extreme and transient thermo-mechanical loads associated with aerodynamic environments that push the structure into a myriad of limit states. Understanding the structural response and eventually structural damage prognosis to assist the design process have been a long-pursuit research focus across industrial and federal agencies [1]. In this work, we are particularly interested in fatigue damage initiation of metallic aerostructures, since the fatigue crack nucleation could take up nearly 90% of the total fatigue life for metals [2].

Existing efforts on investigating the response of aerostructures subjected to high-speed flight environment mainly focus on: 1) characterizing the thermo-mechanical loading associated with high-speed flight; 2) accurate modeling of the material evolution and damage accumulation in the high-speed flight environment. Representative work on characterizing the thermo-mechanical loading include but are not limited to experimental studies by Bebernis et al. [1], Spottswood et al. [3], and numerical investigation with loosely coupling [4], fully-coupling [5, 6] and reduced-order modeling (ROM) [7, 8]. Early research on modeling material response under high-speed flight condition mostly adopted elastic, elastic-plastic models such as the work by Arya et al. [9] and Xue and Mei [10]. More recently, elastic-thermoviscoplastic model [11], the Chaboche constitutive model considering strain hardening together with the Palmgren-Miner linear damage rule [12], viscoelasticviscoplastic formulation accounting for oxygen-assisted

embrittlement [13], creep and multiplicatively-decomposed plasticity [14] have been used to evaluate the response of aerostructures. Given that damage initiation and propagation in metallic material are highly localized phenomena, one needs to track microstructural deformation and consider microstructural mechanisms to capture failure initiation.

Crystal plasticity finite element (CPFE) modeling has been an increasingly used to study microstructure-based plastic deformation, fatigue damage initiation and propagation at different temperatures and loadings [15, 15–19]. However, the tremendous computation cost associated with CPFE simulations, and the orders of magnitude of difference in the length scale between a polycrystalline RVE and a structural component, make it computationally prohibitive to conduct a structural scale CPFE simulation even with parallel computing techniques [20].

To upscale from the microstructure level of polycrystalline representative volume element (RVE) to the structural scale, several homogenization methods have been proposed (e.g., see a detailed review in Ref. [21]). Recently, the eigendeformation-based reduced-order homogenization (EHM) model, originally proposed for fiber-reinforced composites [22–24] has been advanced for the modeling of polycrystal plasticity [25]. EHM is based on the transformation field analysis (TFA) [26] and operates in the context of computational homogenization with a focus on model order reduction of the microscale problem. EHM pre-computes certain microstructure information by solving a series of linear elastic problems defined over the fully resolved microstructure (i.e., concentration tensors, interaction tensors) and approximates the microscale problem using a much smaller basis spanned over subdomains (also called parts) of the RVE. Using this reduced basis, and prescribed spatial variation of inelastic response fields over the parts, the microscale problem leads to a set of algebraic equations with part-wise responses as unknowns, instead of node-wise quantities as in CPFE. EHM has also recently been extended for a sparse formulation to further improve its efficiency and scalability [27], incorporating different lattice structures and dislocation density based flow rule and hardening laws [28], and extension to finite deformation [29].

This work presents a thermo-mechanical EHM for computationally efficient multiscale analysis of polycrystalline structures subjected to thermo-mechanical loading, with its application on a generic aircraft wing panel structure made of titanium alloy, Ti-6Al-2Sn-4Zr-2Mo-0.1Si (Ti-6242S). Section 2 provides an overview of the EHM model accounting for thermo-mechanical loading. Model implementation, calibration and validation are presented in Section 3, followed by the detailed analysis of an aircraft skin panel in Section 4. Section 5 summarize the manuscript.

II. EHM for polycrystalline materials subjected to thermo-mechanical loading

EHM is based on the transformation field theory analysis [26], to reduce the computational cost associated with the microscale problem in a two-scale computational homogenization (also called FE^2 , see [30, 31]) setting as shown in Fig. 1. In standard computational homogenization, one needs to solve the coupled microscale problem (defined over the microscale domain Θ , characterized by spatial coordinate system \mathbf{y}) and the macroscale problem (defined over the macroscale domain Ω , characterized by spatial coordinate system \mathbf{x}). EHM aims at model order reduction

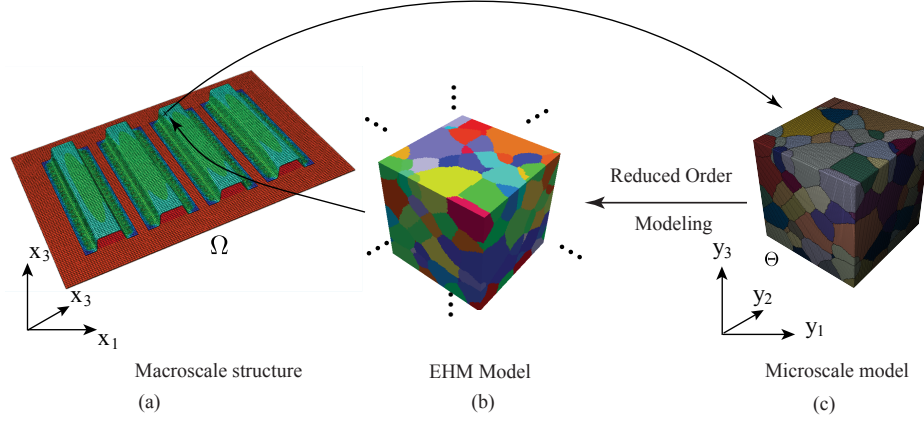


Fig. 1 Multiscale reduced-order modeling framework: (a) macroscale structure, an aerostructure subjected to thermo-mechanical loading, which require evaluation of a full-field microscale problem in c) at any integration point of the macroscale structure at any loading increment in a computational homogenization setting, and instead replaced by a reduced-order representation in b) in an EHM framework.

of the microscale problem by: 1) partitioning the microstructure into a small number of subdomains (or parts), where the coarsest partitioning in the context of crystal plasticity is one-part-per-grain; 2) pre-computing certain microstructural information, including concentration and interaction tensors obtained from linear elastic simulations on the microstructure, associated with the partitioning of the microstructure domain; and 3) prescribing spatial variation of inelastic fields in each part, where uniform response is assumed in each part.

Following the derivation in Ref. [32], we arrive at a one-way coupled thermo-mechanical problem. The thermal problem do not account for the temperature variation over the microstructure, and provides the spatial variation (over the macroscopic coordinate $\mathbf{x} \in \Omega$) and temporal history (over time $t \in [0, t_1]$). The mechanical problem accounts for the response variation over the microstructure, and starting from a coupled micro-macro scale problem, a reduced-order system is derived to replace the microscale problem, serving as a constitutive law for the macroscopic problem. The macroscopic problem is defined as

$$\bar{\sigma}_{ij,j}(\mathbf{x}, T, t) + \bar{b}_i(\mathbf{x}, T, t) = \bar{\rho} \ddot{\bar{u}}_i(\mathbf{x}, T, t) \quad (1)$$

in which $\bar{\mathbf{u}}$ and T denote the macroscopic displacement and temperature fields, respectively. $\bar{\boldsymbol{\sigma}}$ represents the macroscale stress, $\bar{\mathbf{b}}$ the macroscale body force. $\bar{\rho}$ is the homogenized density.

The reduced-order system features a constitutive equation expressed in the form of an algebraic system, which is solved for a small set of inelastic strains associated with each part and expressed as (at an arbitrary material point \mathbf{x} on the structure). The flow rule and hardening rules are also expressed for each reduced-order part. The ROM system are summarized in Box 1, and detailed derivation are provided in Ref. [32].

Given: temperature history $T(t)$, coefficient tensors $M_{ijkl}^{(\alpha\beta)}$, $P_{ijkl}^{(\alpha\beta)}$, $A_{ijkl}^{(\beta)}$, $\mathcal{A}_{ij}^{(\beta)}$, current state (e.g., stress, strain and all internal state variables below), and strain increments $\Delta\bar{\epsilon}_{kl}$

Find: new state at the end of the current loading increment

- Constitutive equation:

$$\sum_{\alpha=1}^n M_{ijkl}^{(\alpha\beta)}(T)\dot{\sigma}_{kl}^{(\alpha)}(\mathbf{x}, T, t) - \sum_{\alpha=1}^n [P_{ijkl}^{(\beta, \alpha)}(T) - \delta^{(\alpha\beta)} I_{ijkl}] \dot{\mu}_{kl}^{(\alpha)}(\mathbf{x}, T, t) = A_{ijkl}^{(\beta)}(T) \dot{\bar{\epsilon}}_{kl}(\mathbf{x}, T, t) + \mathcal{A}_{ij}^{(\beta)}(T) \dot{T}(\mathbf{x}, t)$$

$$\bar{\sigma}_{ij} = \sum_{\beta=1}^n \frac{|\Theta^{(\beta)}|}{|\Theta|} \sigma_{ij}^{(\beta)}$$

- Kinematics:

$$\dot{\mu}_{ij}^{(\alpha)}(\mathbf{x}, t) = \sum_{s=1}^N \dot{\gamma}^{s(\alpha)}(\mathbf{x}, t) Z_{ij}^{s(\alpha)}$$

- Flow rule:

$$\dot{\gamma}^{s(\alpha)}(\mathbf{x}, T, t) = \frac{\rho_m^{s(\alpha)} v_{id}^{s(\alpha)} (b^{s(\alpha)})^2}{2} \exp\left(\frac{(\tau^{s(\alpha)} - s^{s(\alpha)}) \Delta V^{s(\alpha)} - \Delta F^{s(\alpha)}}{kT}\right) \text{sgn}(\tau^{s(\alpha)})$$

- Internal state variables:

$$s^{s(\alpha)}(\mathbf{x}, T, t) = s_0^{s(\alpha)}(\mathbf{x}, T) + s_{\text{for}}^{s(\alpha)}(\mathbf{x}, T, t) + s_{\text{deb}}^{s(\alpha)}(\mathbf{x}, T, t); \quad s_0^{s(\alpha)} = s_{298K}^{s(\alpha)} - s^{s(\alpha)} \left[1 - \exp\left(\frac{T - T_{\text{ref}}^s}{\widehat{T}^{s(\alpha)}}\right) \right]$$

$$s_{\text{deb}}^{s(\alpha)} = \mu^{(\alpha)} b^{s(\alpha)} k_{\text{deb}} \sqrt{\rho_{\text{deb}}^{s(\alpha)}} \ln\left(\frac{1}{b^{s(\alpha)} \sqrt{\rho_{\text{deb}}^{s(\alpha)}}}\right); \quad s_{\text{for}}^{s(\alpha)} = \mu^{(\alpha)} \chi b^{s(\alpha)} \sqrt{\rho_{\text{for}}^{s(\alpha)}}; \quad \rho_{\text{for}}^{s(\alpha)} = \rho_{\text{fwd}}^{s(\alpha)} + \rho_{\text{rev}}^{s+(\alpha)} + \rho_{\text{rev}}^{s-(\alpha)}$$

$$s_{\text{deb}}^{s(\alpha)} = \mu^{(\alpha)} b^{s(\alpha)} k_{\text{deb}} \sqrt{\rho_{\text{deb}}^{s(\alpha)}} \ln\left(\frac{1}{b^{s(\alpha)} \sqrt{\rho_{\text{deb}}^{s(\alpha)}}}\right)$$

- Hardening rules:

$$\frac{\partial \rho_{\text{fwd}}^{s(\alpha)}}{\partial \gamma^{s(\alpha)}} = (1-p) k_1^{s(\alpha)} \sqrt{\rho_{\text{for}}^{s(\alpha)}} - k_2^{s(\alpha)} \rho_{\text{for}}^{s(\alpha)}; \quad d\rho_{\text{deb}}^{s(\alpha)} = \sum_s \frac{\partial \rho_{\text{deb}}^{s(\alpha)}}{\partial \gamma^{s(\alpha)}} d\gamma^{s(\alpha)} = \sum_s q b^{s(\alpha)} \sqrt{\rho_{\text{deb}}^{s(\alpha)}} k_2^{s(\alpha)} \rho_{\text{for}}^{s(\alpha)}$$

$$\frac{\partial \rho_{\text{rev}}^{s+(\alpha)}}{\partial \gamma^{s(\alpha)}} = \begin{cases} p k_1^{s(\alpha)} \sqrt{\rho_{\text{for}}^{s(\alpha)}} - k_2^{s(\alpha)} \rho_{\text{rev}}^{s+(\alpha)} & \tau^{s(\alpha)} > 0 \\ -k_1^{s(\alpha)} \sqrt{\rho_{\text{for}}^{s(\alpha)}} \left(\frac{\rho_{\text{rev}}^{s+(\alpha)}}{\rho_0^{s(\alpha)}}\right)^{\widehat{m}} & \tau^{s(\alpha)} < 0 \end{cases}; \quad \frac{\partial \rho_{\text{rev}}^{s-(\alpha)}}{\partial \gamma^{s(\alpha)}} = \begin{cases} -k_1^{s(\alpha)} \sqrt{\rho_{\text{for}}^{s(\alpha)}} \left(\frac{\rho_{\text{rev}}^{s-(\alpha)}}{\rho_0^{s(\alpha)}}\right)^{\widehat{m}} & \tau^{s(\alpha)} > 0 \\ p k_1^{s(\alpha)} \sqrt{\rho_{\text{for}}^{s(\alpha)}} - k_2^{s(\alpha)} \rho_{\text{rev}}^{s-(\alpha)} & \tau^{s(\alpha)} < 0 \end{cases}$$

- Schmid's law:

$$\tau^{s(\alpha)}(\mathbf{x}, t) = \boldsymbol{\sigma}^{(\alpha)}(\mathbf{x}, t) : \mathbf{Z}^{s(\alpha)} \quad \mathbf{Z}^{s(\alpha)} = \mathbf{n}^{s(\alpha)} \otimes \mathbf{m}^{s(\alpha)}$$

Box 1 Reduced order microscale problem.

III. Model implementation, calibration and validation

The 2D electron backscatter diffraction (EBSD) scan of the microstructure from Ref. [33] is used to extract the statics to generate a 3D polycrystalline RVE [28] using software DREAM.3D [34] following the microstructure reconstruction and meshing procedures detailed in Refs. [35, 36]. Figure 2 shows the orientation and grain size distribution of Ti-6242S and a 145-grain microstructure used in the current study. When constructing the EHM, each grain constitutes a EHM part, leading to 145-part EHM model. The dislocation density based crystal plasticity model

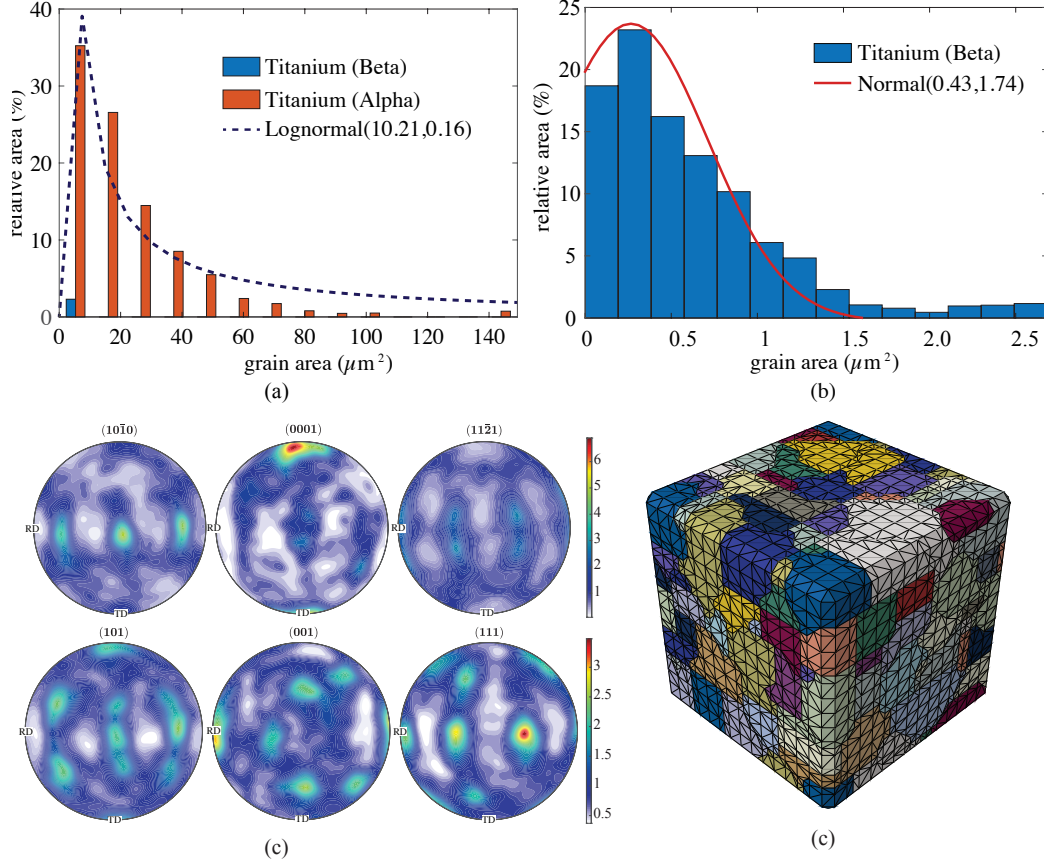


Fig. 2 Microstructure for Ti-6242S: grain size distribution of a) α and b) β phase; c) orientation distribution, and d) a 145-grain microstructure used in the current study. Data was published in Refs.[28, 32].

defined in Box 1 together with the macroscopic equilibrium equation (Eq. (1)), and a given set of initial and boundary conditions fully define the multiscale problem. The influence function needed to compute the coefficient tensors in EHM are first evaluated on the elastic microstructure at different base temperatures [32] to compute the corresponding coefficient tensors. Coefficient tensors at any intermediate temperature can be directly interpolated [37]. A calibration process has been detailed in Ref. [32] using the reconstructed microstructure above, and a list of calibrated model parameters are provided. The calibrated model can well capture the stress-strain response of from Ref. [33], at two different strain rates (quasi-static (QS): 8.33×10^{-5} /s; high strain rate (HS): 0.01/s) and a wide range of temperatures (from 298 to 923 K) as shown in Fig. 3.

IV. A skin panel subjected to thermo-mechanical loading associated with high-speed flight

In this section, the calibrated EHM model for Ti-6242S is utilized to analyze a representative skin panel structure subjected to combined thermo-mechanical loading associated with a high-speed flight condition. This analysis aims at computationally characterizing the deformation processes at both structural and microscopic scale that could be potentially used for fatigue initiation analysis and structural damage prognosis.

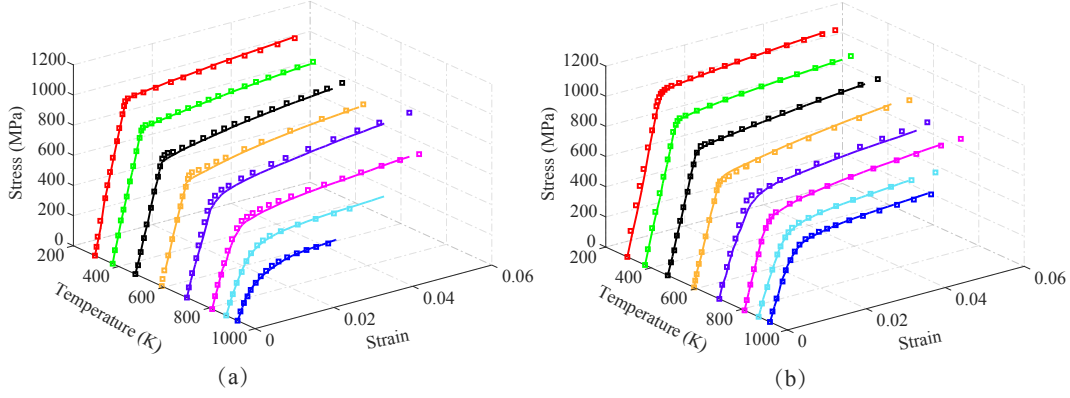


Fig. 3 Validation of the EHM model, with a comparison of the stress-strain response between simulations and experiments across different temperatures at a) quasi-static strain rate, and b) high strain rate. Data was published in Ref.[32].

A. Representative skin panel structure

A generic skin panel that has been previously investigated in the literature [3, 5, 6, 38, 39] is used in this study. The panel has a dimension of $305.8 \times 254 \times 0.5$ mm, with stiffeners along the long edges, and is made of Ti-6242S. The width of the stiffeners is 30 mm and the thickness is 0.021 mm. The panel is discretized with tri-linear eight-noded hexahedron elements with reduced integration that are regularized with hourglass stiffness, and the stiffeners are discretized with four-noded shell elements with reduced integration. In the current simulations, the stiffeners are taken to be elastic, while for the panel the EHM for Ti-6242S based on the 145-grain microstructure is adopted. A time step size and mesh size convergence study has been conducted in Ref. [32], confirming that the element size of $h = 3.175$ mm and time step size of $\Delta t = 5e - 6$ s yield a converged response and will be employed in all the simulations afterwards. A revised version of the panel with three bolt holes is shown in Fig. 4 (a) along edge AD is also considered in the current study. An optimal time step size is determined based on a time step convergence study in Ref. [32].

The panel is subjected to thermo-mechanical loading associated with a Mach 2, free-stream dynamic pressure of 123 KPa [3]. To obtain the spatially varying temperature profile over the panel, a thermal analysis of the panel subjected to a free stream temperature is used following Ref. [38]. In the current study, we start with the temperature profile of the panel at $t=20$ s after imposing the adiabatic wall temperature, and conduct a thermo-mechanical analysis for 20 ms using EHM. At the beginning of the simulation (i.e., 20 s after aerodynamic heating), the calculated temperature profile is shown in Fig. 4 (b), with a temperature range of approximately 300-385 K, similar to that in Ref. [40]. We note that since within the current temperature range the change in elastic moduli is negligible, we directly use the values at room temperature from [41] to save computational cost. If the temperature range is large, the dependency of elastic moduli on temperature reported in Ref. [16] can be considered. Within the 20 ms span of the analysis, temporal temperature change is relatively small, therefore we consider $\dot{T} = 0$ in the constitutive equation of Box 1.

The pressure applied on the panel consists of a mean pressure and a temporally and spatially varying acoustic part.

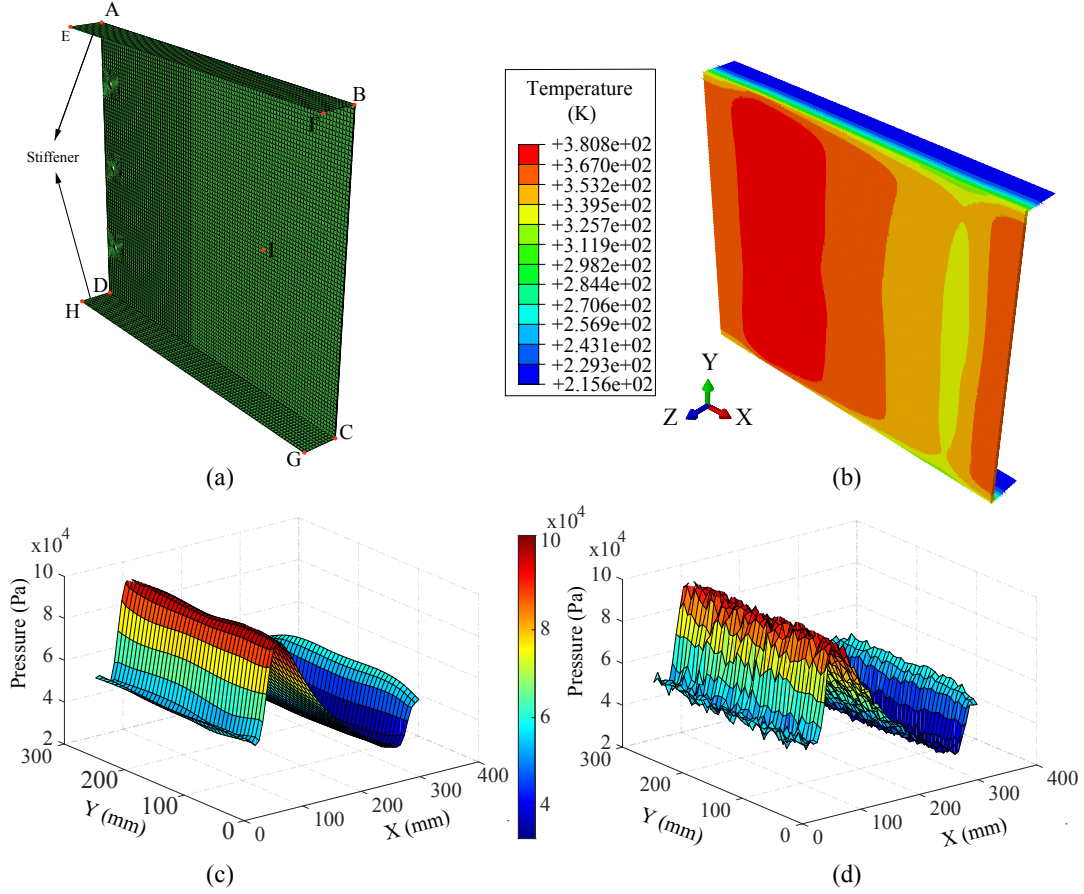


Fig. 4 Panel structure subjected to thermo-mechanical loading: a) mesh of the panel; b) temperature distribution over the panel; c) mean pressure and d) total pressure at time 0.01s. Data was published in Ref.[32].

The mean pressure is obtained from a steady state CFD calculation using Reynolds-Averaged Navier-Stokes (RANS) equations for flow on a rigid panel (see Ref. [38] for details) as shown in Fig. 4 (c). The acoustic part is the turbulent boundary layer (TBL) pressure on the panel, approximated using a series of random cosine functions to generate the spatial and temporal distributions. The number of cosine functions and magnitude of each cosine function are estimated from the work of Spottswood et al. [3], while frequency are randomly chosen between 1 and 500 Hz. This total pressure profile obtained by the summation of the steady state pressure and the acoustic part is shown in Fig. 4 (d), and is consistent with the reported numerical and experimental results in Refs. [6, 39].

B. Structural scale response investigation: effects of temperature

To understand the effect of temperature on the response of the panel (Fig. 4 (a)), we consider both uniform (case 1) and spatially varying (case 2) temperatures. In case 1, the temperature of the structure is 473.15 K everywhere, while in case 2, the temperature profile shown in Fig. 4 (b) is used. To promote the plastic deformation, a factor of 5 is multiplied to the pressure profile for this panel without bolt holes.

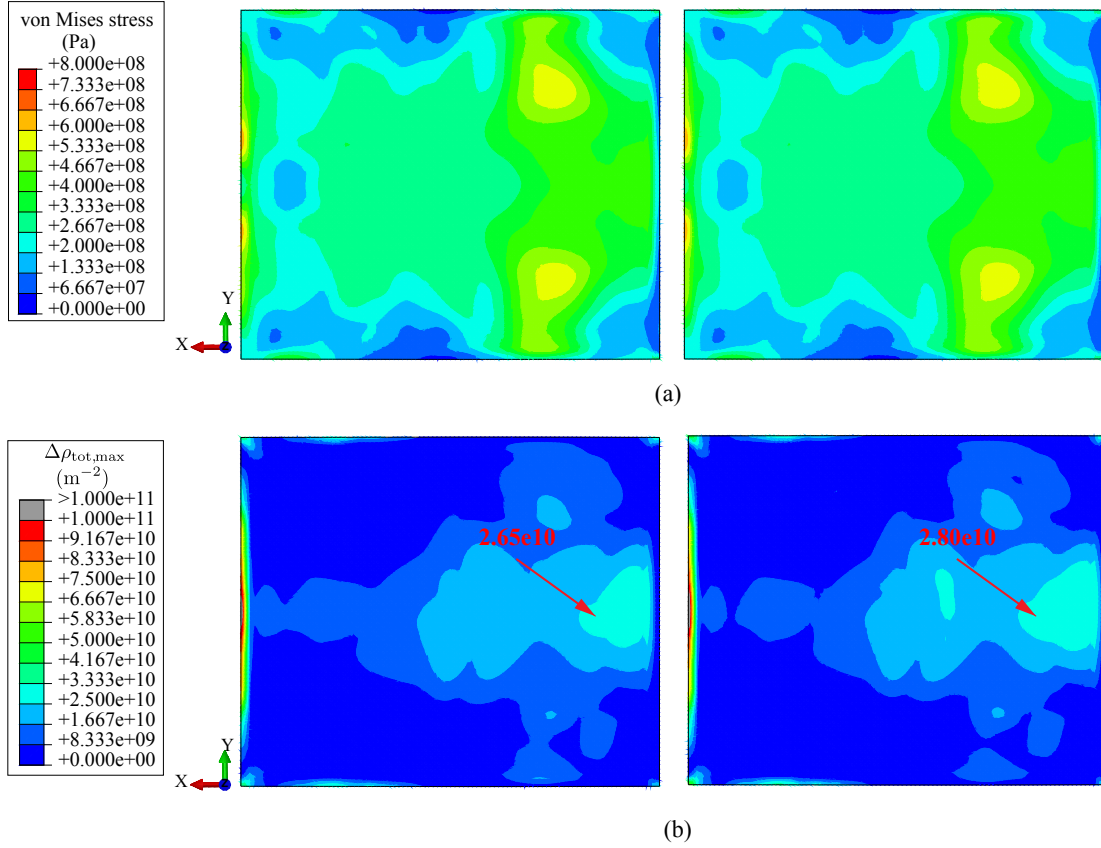


Fig. 5 Comparison between cases 1 (left) and 2 (right): a) von Mises stress; b) maximum dislocation density discrepancy. Data was published in Ref.[32].

Joseph et al. [42, 43] observed that there are intense dislocation pile-ups at the grain boundaries slightly underneath the crack nucleation surface of fatigued Ti-6242S using transmission electron microscopy. This observation leads to the proposal of using the maximum dislocation density discrepancy (MD³) between neighboring grains as a fatigue indicator parameter (FIP) for Ti-6242 [28, 44]. This FIP finds the maximum sessile dislocation density discrepancy across all grain pairs within the microstructure, $\Delta\rho_{tot,max}$ following the procedures in Ref. [28].

We track both macroscale and the microstructure response (i.e., one uniform response per grain in the current EHM) associated with each structural scale integration point, and compare the von-Mises stress and the maximum dislocation density discrepancy in Fig. 5 between cases 1 and 2. The stress comparison in Fig. 5 shows that the primary stress concentration region is close to the constrained edge, with several additional (secondary) stress concentration regions within the panel. In the secondary concentration regions in the panel, case 1 has slightly larger stress. While case 1 has much higher temperature than case 2, the resulting stress in the two simulations are of similar magnitude. When examining the maximum dislocation discrepancy, $\Delta\rho_{tot,max}$, in the concentration region in the panel in Fig. 5, it is observed that case 2 has an $\Delta\rho_{tot,max}$ value 5.7% higher than that in case 1. This suggests that the spatial variation in temperature gradients promotes the fatigue initiation at the microscale. While current experimental investigation of

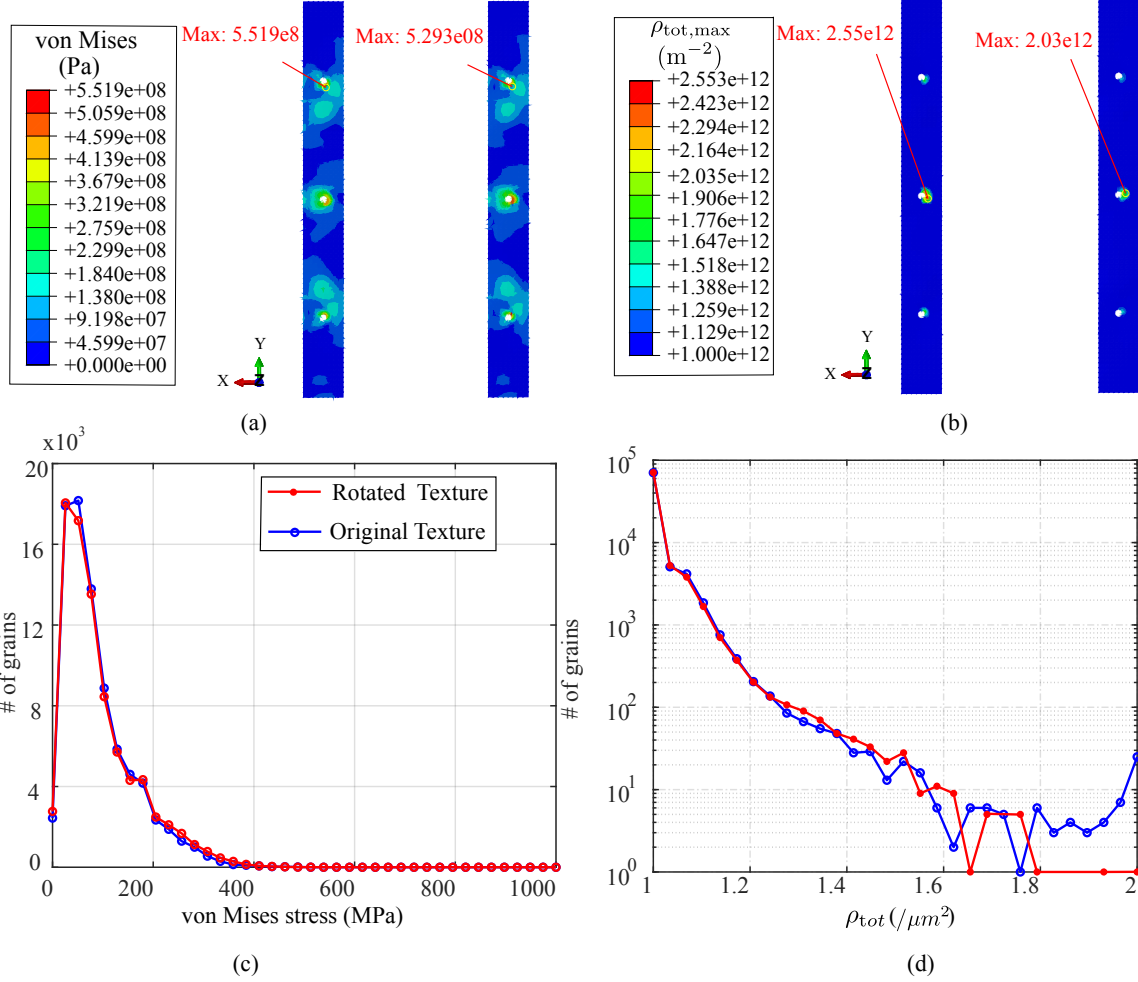


Fig. 6 Response of the bolted panel: a) von Mises stress; and b) maximum dislocation density discrepancy at the end of the simulation using the original (left) and rotated (right) texture; histogram of the microscale stress c) and total dislocation density d) associated with the elements around the middle hole. Data was published in Ref.[32].

the panel response has not yet gone down to the subgrain level, it has been demonstrated that the presence of thermal gradients will shift the boundary layer transient, alter the panel response [45] and facilitate the plate buckling [46]. The promotion of fatigue initiation by thermal gradient has also been reported for nickel-based alloy [47, 48].

C. Local response investigation and fatigue initiation site prediction: effect of texture

We further investigate the behavior in the areas of localized stress concentrations by moving to the panel with bolt holes and constrain the displacements of all nodes on the inner faces of the bolt holes to introduce localization. In addition to the original texture, we also investigate a case with a rotated texture, by reorienting the dominant c-axis direction from along the panel length direction to along the width direction to study the impact of texture on fatigue initiation. We note that it is also possible to have different regions of the panel to have different textures or microstructures resulting from different manufacturing processes, such that high stress, strain and fatigue initiation

locations can be altered and achieve different fatigue life [28].

The von-Mises stress and maximum dislocation discrepancy around the holes are shown in Fig. 6 (a)-(b). The stress and the maximum dislocation discrepancy all show higher values around the bolt holes. The macroscale response measures such as stress show are very close between the two textures. However, for microscale response such as $\Delta\rho_{\text{tot,max}}$ show significant differences. This result demonstrates the presence of localized phenomenon, which are undetectable by homogenized measures.

To better probe the local response, we focus on a square region ($2.54\text{cm} \times 2.54\text{cm}$) around the center bolt hole (Fig. 7 (a)). This region contains 576 elements, hence the response of 83,520 grains are tracked. The histograms of stress and dislocation density in each grain are plotted in Fig. 6 (c)-(d). Since the histograms have very long tails, the values beyond a certain magnitude are grouped into the last bin for better visualization.

It is again clearly shown in Fig. 7 that while the von Mises stress distributions are close between the original and rotated texture, the ρ_{tot} have more significant differences, especially at the tail. For example, in the rotated texture case, there are only four grains that have ρ_{tot} higher than $1.8\ \mu\text{m}^{-2}$. In contrast, there are more than twenty grains that above ρ_{tot} higher than $2.0\ \mu\text{m}^{-2}$ in the original texture case. Since fatigue damage initiation is dictated by extreme values at the microstructure scale, this difference suggests that texture could play an important role in fatigue initiation.

Figure 7 (a) shows the same grain pair exhibits the largest ρ_{tot} in both texture cases, and Figure 7 (b) shows the corresponding structural locations in the panel which are different. The locations of the most critical points in the original and rotated texture cases are very close to each other, and close to the hole as shown in Fig. 7 (b). The magnitude in the original texture case is approximately 50% higher than that of the rotated texture. It has been recognized both computationally and experimentally that texture has a significant role on the plastic response, and it is possible to use small clusters of similar crystal orientations, called micro-textured regions (MTR) or macrozones to change the fatigue sensitivities in titanium alloys [49, 50]. EHM could be potentially used to spatially design those MTR to improve the fatigue resistance of a given structural component. The orientations of this grain pair, are represented using two hexagonal prisms as shown in Fig. 7 (c), where the normal to the base of the prism is the c-axis of the grain. This example demonstrates the capability of EHM predicting failure initiation at a structural material point, by tracking the most critical grain pair inside the microstructure associated with that structural location.

V. Summary

This manuscript presented a multiscale reduced-order homogenization model for titanium structures subjected to thermo-mechanical loading associated with high-speed flight, which concurrently track the structural and underlying microscale response, enabling microstructure-informed fatigue damage initiation prediction. This development is an extension of the EHM model by incorporating thermal strains at the microscale, and accounts for temperature dependent material properties and evolution laws. The developed model was fully calibrated and can accurately capture the stress-

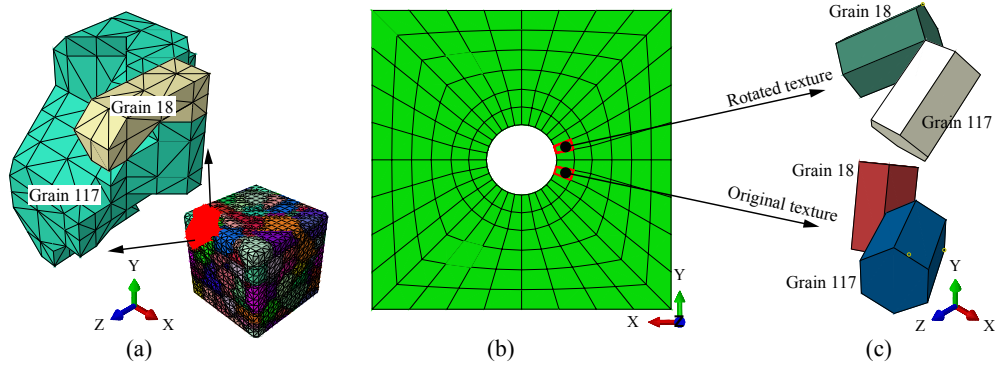


Fig. 7 Effects of the texture on fatigue initiation site suggested by $\Delta\rho_{\text{tot,max}}$: location of a) critical grain pair; b) critical structural location; c) orientations of the critical grain pair for the original and rotated texture. Data was published in Ref.[32]

strain response of titanium materials under uniaxial tension across a wide range of temperature and strain rates. A generic airplane skin panel subjected to thermo-mechanical loading associate with high-speed flight was then analyzed using the calibrated model to evaluate its response. The model demonstrates its capability for determining potential structural scale fatigue initiation sites, and pinpointing the initiation sites within the underlying microstructure.

Funding Sources

The authors gratefully acknowledge the research funding from the Air Force Office of Science Research Multi-Scale Structural Mechanics and Prognosis Program (Grant No: FA9550-13-1-0104). We also acknowledge the technical cooperation of the Structural Science Center of the Air Force Research Laboratory. M. Lin and X. Zhang have been financially supported by the faculty start-up funding from the University of Wyoming, which is also gratefully acknowledged.

References

- [1] Bebernis, T., Spottswood, S., Perez, R., and Eason, T., “Nonlinear Response of a Thin Panel in a Multi-Discipline Environment: Part I – Experimental Results,” *Nonlinear Dynamics, Volume 1*, Springer, 2016, pp. 237–248. https://doi.org/10.1007/978-3-319-29739-2_22.
- [2] Bache, M. R., “A review of dwell sensitive fatigue in titanium alloys: the role of microstructure, texture and operating conditions,” *Int. J. Fatigue*, Vol. 25, No. 9, 2003, pp. 1079–1087. [https://doi.org/10.1016/S0142-1123\(03\)00145-2](https://doi.org/10.1016/S0142-1123(03)00145-2).
- [3] Spottswood, S. M., Bebernis, T., and Eason, T., “Full-field, dynamic pressure and displacement measurements of a panel excited by shock boundary-layer interaction,” *19th AIAA/CEAS aeroacoustics conference*, 2013, p. 2016. <https://doi.org/10.2514/6.2013-2016>.
- [4] Perez, R. A., Spottswood, S. M., Bebernis, T. J., Bartram, G. W., and Eason, T. G., “Nonlinear Dynamic Response Prediction

- of a Thin Panel in a Multi-Discipline Environment: Part II—Numerical Predictions,” *Nonlinear Dynamics, Volume 1*, Springer, Cham, Switzerland, 2016, pp. 249–257. https://doi.org/10.1007/978-3-319-29739-2_23.
- [5] Culler, A. J., and McNamara, J. J., “Impact of fluid-thermal-structural coupling on response prediction of hypersonic skin panels,” *AIAA J.*, Vol. 49, No. 11, 2011, pp. 2393–2406. <https://doi.org/10.2514/1.J050617>.
- [6] Gogulapati, A., Deshmukh, R., McNamara, J. J., Vyas, V., Wang, X., Mignolet, M. P., Bebernis, T., Spottswood, S. M., and Eason, T. G., *Response of a Panel to Shock Impingement: Modeling and Comparison with Experiments-Part 2*, 2015. <https://doi.org/10.2514/6.2015-0685>.
- [7] Crowell, A. R., and McNamara, J. J., “Model Reduction of Computational Aerothermodynamics for Hypersonic Aerothermoelasticity,” *AIAA J.*, 2012. <https://doi.org/10.2514/1.J051094>.
- [8] Gogulapati, A., Brouwer, K. R., Wang, X., Murthy, R., McNamara, J. J., and Mignolet, M. P., *Full and Reduced Order Aerothermoelastic Modeling of Built-Up Aerospace Panels in High-Speed Flows*, 2020. <https://doi.org/10.2514/6.2017-0180>.
- [9] Arya, V. K., Melis, M. E., and Halford, G. R., “Finite Element Elastic-Plastic-Creep and Cyclic Life Analysis of a Cowl Lip,” *Fatigue Fract. Eng. Mater. Struct.*, Vol. 14, No. 10, 1991, pp. 967–977. <https://doi.org/10.1111/j.1460-2695.1991.tb00006.x>.
- [10] Xue, D. Y., and Mei, C., “Finite element nonlinear flutter and fatigue life of two-dimensional panels with temperature effects,” *J. Aircr.*, Vol. 30, No. 6, 1993, pp. 993–1000. <https://doi.org/10.2514/3.46444>.
- [11] Sobotka, J. C., Oral, A., and Culler, A. J., “Towards a coupled loads-response-life prediction framework for hypersonic structures in combined extreme environments,” *54th AIAA/ASME/ASCE/AHS/ASC Structures, Structural Dynamics, and Materials Conference*, 2013, p. 1519. <https://doi.org/10.2514/6.2013-1519>.
- [12] Miner, A., “Cumulative damage in fatigue,” 1945.
- [13] Oskay, C., and Haney, M., “Computational modeling of titanium structures subjected to thermo-chemo-mechanical environment,” *Int. J. Solids Struct.*, Vol. 47, No. 24, 2010, pp. 3341–3351. <https://doi.org/10.1016/j.ijsolstr.2010.08.014>.
- [14] Clough, J. L., Oberai, A. A., and Camberos, J. A., *Deformation of a Panel in Repeated High Speed Flow Modeled with Creep and Multiplicatively-Decomposed Plasticity*, 2020. <https://doi.org/10.2514/6.2020-2418>.
- [15] Meissonnier, F., Busso, E., and O’Dowd, N., “Finite element implementation of a generalised non-local rate-dependent crystallographic formulation for finite strains,” *Int. J. Plast.*, Vol. 17, No. 4, 2001, pp. 601–640. [https://doi.org/10.1016/S0749-6419\(00\)00064-4](https://doi.org/10.1016/S0749-6419(00)00064-4).
- [16] Ozturk, D., Shahba, A., and Ghosh, S., “Crystal plasticity FE study of the effect of thermo-mechanical loading on fatigue crack nucleation in titanium alloys,” *Fatigue Fract. Eng. Mater. Struct.*, Vol. 39, No. 6, 2016, pp. 752–769. <https://doi.org/10.1111/ffe.12410>.

- [17] Hu, P., Liu, Y., Zhu, Y., and Ying, L., “Crystal plasticity extended models based on thermal mechanism and damage functions: Application to multiscale modeling of aluminum alloy tensile behavior,” *Int. J. Plast.*, Vol. 86, 2016, pp. 1–25. <https://doi.org/10.1016/j.ijplas.2016.07.001>.
- [18] Liu, Y., Zhu, Y., Oskay, C., Hu, P., Ying, L., and Wang, D., “Experimental and computational study of microstructural effect on ductile fracture of hot-forming materials,” *Mat. Sci. Eng. A*, Vol. 724, 2018, pp. 298 – 323. <https://doi.org/https://doi.org/10.1016/j.msea.2018.03.049>.
- [19] Benzinger, J., Liu, Y., Zhang, X., Luecke, W., Ponge, D., Dutta, A., Oskay, C., Raabe, D., and Wittig, J., “Experimental and numerical study of mechanical properties of multi-phase medium-Mn TWIP-TRIP steel: Influences of strain rate and phase constituents,” *Acta Mater.*, Vol. 177, 2019, pp. 250 – 265. <https://doi.org/10.1016/j.actamat.2019.07.036>.
- [20] Bishop, J. E., Emery, J. M., Field, R. V., Weinberger, C. R., and Littlewood, D. J., “Direct numerical simulations in solid mechanics for understanding the macroscale effects of microscale material variability,” *Comput. Methods Appl. Mech. Eng.*, Vol. 287, 2015, pp. 262–289. <https://doi.org/10.1016/j.cma.2015.01.017>.
- [21] Matouš, K., Geers, M. G., Kouznetsova, V. G., and Gillman, A., “A review of predictive nonlinear theories for multiscale modeling of heterogeneous materials,” *Journal of Computational Physics*, Vol. 330, 2017, pp. 192–220. <https://doi.org/10.1016/j.jcp.2016.10.070>.
- [22] Oskay, C., and Fish, J., “Eigendefor-mation-based reduced order homogenization for failure analysis of heterogeneous materials,” *Comput. Methods Appl. Mech. Engrg.*, Vol. 196, 2007, pp. 1216–1243. <https://doi.org/10.1016/j.cma.2006.08.015>.
- [23] Crouch, R., and Oskay, C., “Symmetric Mesomechanical Model for Failure Analysis of Heterogeneous Materials,” *Int. J. Multiscale Comput. Eng.*, Vol. 8, No. 5, 2010, pp. 447–461. <https://doi.org/10.1615/IntJMultCompEng.v8.i5.20>.
- [24] Sparks, P., and Oskay, C., “The Method of Failure Paths for Reduced-Order Computational Homogenization,” *Int. J. Multiscale Comput. Eng.*, Vol. 14, 2016. <https://doi.org/10.1615/IntJMultCompEng.2016018702>.
- [25] Zhang, X., and Oskay, C., “Eigenstrain based reduced order homogenization for polycrystalline materials,” *Comput. Methods Appl. Mech. Engrg.*, Vol. 297, 2015, pp. 408–436. <https://doi.org/10.1016/j.cma.2015.09.006>.
- [26] Dvorak, G. J., “Transformation Field Analysis of Inelastic Composite Materials,” *Proc. R. Soc. Lond. A*, Vol. 437, 1992, pp. 311–327. <https://doi.org/10.1098/rspa.1992.0063>.
- [27] Zhang, X., and Oskay, C., “Sparse and scalable eigenstrain-based reduced order homogenization models for polycrystal plasticity,” *Comput. Methods Appl. Mech. Eng.*, Vol. 326, 2017, pp. 241–269. <https://doi.org/10.1016/j.cma.2017.07.027>.
- [28] Liu, Y., Zhang, X., Zhu, Y., Hu, P., and Oskay, C., “Dislocation density informed eigenstrain based reduced order homogenization modeling: verification and application on a titanium alloy structure subjected to cyclic loading,” *Modell. Simul. Mater. Sci. Eng.*, Vol. 28, 2020, p. 025004. <https://doi.org/10.1088/1361-651x/ab602e>.

- [29] Xia, D., Zhang, X., and Oskay, C., “Large-deformation reduced order homogenization of polycrystalline materials,” *Comput. Methods Appl. Mech. Engg.*, Vol. 387, 2021, p. 114119. <https://doi.org/10.1016/j.cma.2021.114119>.
- [30] Feyel, F., and Chaboche, J.-L., “FE2 multiscale approach for modelling the elastoviscoplastic behaviour of long fibre SiC/Ti composite materials,” *Comput. Methods Appl. Mech. Eng.*, Vol. 183, 2000, pp. 309–330. [https://doi.org/10.1016/S0045-7825\(99\)00224-8](https://doi.org/10.1016/S0045-7825(99)00224-8).
- [31] Feyel, F., “A multilevel finite element method (FE^2) to describe the response of highly non-linear structures using generalized continua,” *Comput. Methods Appl. Mech. Eng.*, Vol. 192, 2003, pp. 3233–3244. [https://doi.org/10.1016/S0045-7825\(03\)00348-7](https://doi.org/10.1016/S0045-7825(03)00348-7).
- [32] Zhang, X., Liu, Y., and Oskay, C., “Multiscale Reduced-Order Modeling of a Titanium Skin Panel Subjected to Thermomechanical Loading,” *AIAA Journal*, 2021. <https://doi.org/10.2514/1.J060497>.
- [33] Gockel, B. T., Kolesar, R. S., and Rollett, A. D., “Experimental study of an aerospace titanium alloy under various thermal and tensile loading rate conditions,” *Integr. Mater. Manuf. Innov.*, Vol. 5, No. 1, 2016, p. 13. <https://doi.org/10.1186/s40192-016-0057-0>.
- [34] Groeber, M., and Jackson, M., “DREAM.3D: A Digital Representation Environment for the Analysis of Microstructure in 3D,” *Integr. Mater. Manuf. Innov.*, Vol. 3, 2014, pp. 5–19. <https://doi.org/10.1186/2193-9772-3-5>.
- [35] Zhang, X., and Oskay, C., “Polycrystal plasticity modeling of nickel-based superalloy IN 617 subjected to cyclic loading at high temperature,” *Modelling Simul. Mater. Sci. Eng.*, Vol. 24, 2016, p. 055009. <https://doi.org/10.1088/0965-0393/24/5/055009>.
- [36] Phan, V.-T., Zhang, X., Li, Y., and Oskay, C., “Microscale modeling of creep deformation and rupture in Nickel-based superalloy IN 617 at high temperature,” *Mech. Mater.*, Vol. 114, 2017, pp. 215–227. <https://doi.org/10.1016/j.mechmat.2017.08.008>.
- [37] Zhang, S., and Oskay, C., “Reduced order variational multiscale enrichment method for thermo-mechanical problems,” *Comput. Mech.*, Vol. 59, No. 6, 2017, pp. 887–907. <https://doi.org/10.1007/s00466-017-1380-9>.
- [38] Culler, A. J., “Coupled fluid-thermal-structural modeling and analysis of hypersonic flight vehicle structures,” Ph.D. thesis, The Ohio State University, 2010.
- [39] Gogulapati, A., Deshmukh, R., Crowell, A. R., McNamara, J. J., Vyas, V., Wang, X., Mignolet, M., Bebernis, T., Spottswood, S. M., and Eason, T. G., *Response of a Panel to Shock Impingement: Modeling and Comparison with Experiments*, 2014. <https://doi.org/10.2514/6.2014-0148>.
- [40] Matney, A., Mignolet, M. P., Spottswood, S. M., Culler, A. J., and McNamara, J. J., “Thermal reduced order model adaptation to aero-thermo-structural interactions,” *Proceedings of the 55th Structures, Structural Dynamics and Materials Conference (SciTech 2014), National Harbor, Maryland*, 2014, pp. 13–17. <https://doi.org/10.2514/6.2014-0493>.
- [41] Deka, D., Joseph, D. S., Ghosh, S., and Mills, M. J., “Crystal plasticity modeling of deformation and creep in polycrystalline Ti-6242,” *Metall. Mater. Trans. A*, Vol. 37, 2006, pp. 1371–1388. <https://doi.org/10.1007/s11661-006-0082-2>.

- [42] Joseph, S., Bantounas, I., Lindley, T. C., and Dye, D., “Slip transfer and deformation structures resulting from the low cycle fatigue of near-alpha titanium alloy Ti-6242Si,” *Int. J. Plast.*, Vol. 100, 2018, pp. 90 – 103. <https://doi.org/10.1016/j.ijplas.2017.09.012>.
- [43] Joseph, S., Lindley, T. C., and Dye, D., “Dislocation interactions and crack nucleation in a fatigued near-Alpha titanium alloy,” *Int. J. Plast.*, Vol. 110, 2018, pp. 38–56. <https://doi.org/10.1016/j.ijplas.2018.06.009>.
- [44] Liu, Y., Zhang, X., and Oskay, C., “A comparative study on initiation parameters for near-alpha titanium alloys,” *Submitted*, 2021.
- [45] Riley, Z. B., and McNamara, J. J., “Interaction Between Compliant Structures and Boundary-Layer Transition in Hypersonic Flow,” *AIAA J.*, 2017. <https://doi.org/10.2514/1.J055521>.
- [46] Thornton, E. A., Coyle, M. F., and McLeod, R. N., “Experimental study of plate buckling induced by spatial temperature gradients,” *J. Therm. Stresses*, Vol. 17, No. 2, 1994, pp. 191–212. <https://doi.org/10.1080/01495739408946255>.
- [47] Brendel, T., Affeldt, E., Hammer, J., and Rummel, C., “Temperature gradients in TMF specimens. Measurement and influence on TMF life,” *Int. J. Fatigue*, Vol. 30, No. 2, 2008, pp. 234–240. <https://doi.org/10.1016/j.ijfatigue.2007.01.039>.
- [48] Sun, J., Yuan, H., and Vormwald, M., “Thermal gradient mechanical fatigue assessment of a nickel-based superalloy,” *Int. J. Fatigue*, Vol. 135, 2020, p. 105486. <https://doi.org/10.1016/j.ijfatigue.2020.105486>.
- [49] Echlin, M. P., Stinville, J. C., Miller, V. M., Lenthe, W. C., and Pollock, T. M., “Incipient slip and long range plastic strain localization in microtextured Ti-6Al-4V titanium,” *Acta Mater.*, Vol. 114, 2016, pp. 164–175. <https://doi.org/10.1016/j.actamat.2016.04.057>.
- [50] Liu, Y., and Dunne, F. P. E., “The mechanistic link between macrozones and dwell fatigue in titanium alloys,” *Int. J. Fatigue*, Vol. 142, 2021, p. 105971. <https://doi.org/10.1016/j.ijfatigue.2020.105971>.